Chaotic Mixing and Transport Barriers in an Idealized Stratospheric Polar Vortex

RYO MIZUTA AND SHIGEO YODEN

Department of Geophysics, Kyoto University, Kyoto, Japan

(Manuscript received 19 November 1999, in final form 7 February 2001)

ABSTRACT

Chaotic mixing processes and transport barriers around the wintertime stratospheric polar vortex are investigated with an idealized barotropic model, previously used by Ishioka and Yoden. A barotropically unstable jet is forced in order to obtain a fluctuating polar vortex. A flow with quasiperiodic time dependence and an aperiodic flow with similar behavior are investigated using several Lagrangian methods.

A typical chaotic mixing process is observed in the quasiperiodic flow, resulting in effective mixing inside and outside of the polar vortex. The mixing regions are on the critical latitudes of several planetary waves that grow through barotropic instability. Poincaré sections give accurate locations of chaotic mixing regions, and transport barriers are identified as the edges of invariant torus regimes. In addition to the transport barriers associated with strong potential vorticity gradients, another type of transport barrier exists, which is not related to the steep potential vorticity gradient.

Chaotic mixing is dominant also in the aperiodic flow. Comparing with the quasiperiodic flow, an aperiodic flow with the same wave energy has a higher average Lyapunov exponent. This arises because the area involved in chaotic zones increases. The evolution of the correlation function is also more typical of a chaotic zone. Isolated regions are found near the center of the polar vortex, which can be explained by the invariant tori in the Poincaré sections of the quasiperiodic flow. Implications of the results for the observed ''4-day wave'' in the upper stratosphere are discussed.

1. Introduction

Dynamical processes of transport and mixing around the wintertime stratospheric polar vortex have been examined in connection with the Antarctic ozone hole (e.g., Schoeberl and Hartmann 1991). A transport barrier exists at the edge of the polar vortex and air within the vortex is isolated from outside. This type of polar vortex is known as a ''containment vessel'' (Juckes and McIntyre 1987; Schoeberl et al. 1992). Outside of the vortex is a well-mixed region called the ''surf zone,'' where the potential vorticity (PV) is homogenized on planetary wave breaking events; see McIntyre and Palmer (1983) and McIntyre (1989), who pointed out that the barrier is associated with a steep gradient of PV by the planetary wave restoring mechanism. Mixing occurs also inside the vortex, but is not so strong as outside, depending on hemisphere, altitude, and time of year (Pierce et al. 1994; Waugh et al. 1994).

Studies on isentropic trajectories by using analyzed winds (Bowman 1993) and three-dimensional models (Pierce and Fairlie 1993) showed that chaotic mixing occurs inside and outside of the vortex, respectively, based on the exponential growth of material contours and the patterns of stretching and folding, although there is some difficulty in removing the effect of irregular behavior of wind field itself when applying theoretical analyses of chaotic mixing to such realistic wind fields. Chaotic mixing is a rather new concept introduced in the 1980s (Aref 1984; Ottino 1989): it is an irregular, stochastic behavior of Lagrangian motion of fluid particles in regular flows.

Pierrehumbert (1991a,b) applied the concept of chaotic mixing to geophysical flows; he investigated a planetary wave motion with a small periodic perturbation in a two-dimensional channel domain and showed the evidence of chaotic mixing in the flow. Mixing in two-dimensional nondivergent flows has been studied in relation with Hamiltonian dynamics for fluid particles. Some other kinematical studies motivated by atmospheric and oceanic flows also revealed chaotic motions of fluid in planetary waves (Samelson 1992; del-Castillo-Negrete and Morrison 1993; Duan and Wiggins 1996). However, discrepancy between time-periodic behavior of the velocity field and chaotic behavior of PV gives rise to the question as to whether such kinematical models are consistent with dynamically generated phenomena. This is called the dynamical consistency problem (Ngan and Shepherd 1997). To get an answer to the problem, Ngan and Shepherd (1997) used a vorticity-conserving equation and investigated chaotic mixing

Corresponding author address: Shigeo Yoden, Department of Geophysics, Kyoto University, Kyoto 606-8502, Japan.
E-mail: yoden@kugi.kyoto-u.ac.jp

and transport in a nonlinear Rossby wave critical layer flow. They argued that the velocity is associated with the coarse-grained vorticity and that the fine-grained vorticity behaves as a tracer.

In this study, the stratospheric polar vortex is idealized as a solution with quasiperiodic time dependence of a nondivergent barotropic model, and horizontal mixing around the vortex is investigated. The time periodicity enables us to use the same kind of analysis methods as in the kinematical studies of Hamiltonian dynamics. The flow field in our model has dynamical consistency because it is obtained in a direct numerical simulation of a full dynamical equation more akin to the atmosphere than previous kinematical models. In addition, the mixing process in the quasiperiodic flow is compared with that in a more realistic aperiodic flow of similar pattern that is obtained in the same model.

In the flows of our model, eastward propagating planetary waves generated through barotropic instability are dominant. The situation is close to that in the upper stratosphere of the Southern Hemisphere where the 4-day wave is often observed. The 4-day wave appears in the upper stratosphere in winter (Venne and Stanford 1979), more evidently in the Southern Hemisphere than in the Northern Hemisphere. It is dominated by zonal wavenumbers from 1 to 4, traveling eastward with the same phase speed. Observational and theoretical studies are summarized in Allen et al. (1997), and Manney et al. (1998). Hartmann (1983) examined linear stability of idealized zonal jet profiles and pointed out that the barotropic instability of the polar night jet can cause the 4-day wave. Manney et al. (1988) investigated the barotropic instability of the observed jet profiles in the Southern Hemisphere winter and found good agreement with the characteristics of the observed wave. Bowman and Chen (1994), and Orsolini and Simon (1995) investigated the mixing in barotropic models in which unstable modes similar to the 4-day wave develop. They used analytical jet profiles introduced by Hartmann (1983) as initial conditions and examined transient evolutions from the zonally symmetric flows. Here we use the same kind of profiles as a zonally symmetric wind forcing. The effects of the forcing maintaining the unstable jet and the dissipation corresponding to the radiative damping are taken into consideration for a more realistic situation in the winter stratosphere.

The two-dimensional barotropic model is described in section 2. Analyses on the flow fields and the mixing process comparing a quasiperiodic solution and an aperiodic one are shown in section 3. Discussion including relevance to the real atmosphere is given in section 4, and conclusions are in section 5.

2. Model

A model of a two-dimensional nondivergent flow on a rotating sphere with forcing and dissipation is considered following Ishioka and Yoden (1995). The system is governed by a vorticity equation:

$$\frac{Dq}{Dt} = -\alpha(q - \overline{q}_0) + \nu\left(\nabla^2 + \frac{2}{a^2}\right)(q - \overline{q}_0), \quad (1)$$

where q is the PV (or, the absolute vorticity in this case), defined as $q \equiv \nabla^2\psi + 2\Omega \sin\phi$. Here, ψ is the streamfunction, ∇^2 is the horizontal Laplacian operator, Ω is the angular speed of the earth's rotation, and ϕ is latitude. The first term on the right-hand side is a relaxation term to a prescribed zonally symmetric $\overline{q}_0$ defined below (hereafter overbar denotes zonal mean), which mimics the radiative forcing of a zonally symmetric vortex motion. The relaxation time α^{-1} is set to 10 days. The second term is an artificial small viscosity with $\nu = 6.43 \times 10^4$ m^2 s^{-1}, and a is the radius of the earth. The PV is not conserved following the motion mainly by the external forcing.

A spectral model with T85 truncation is used and the advection term is computed with the transform method of 128° lat × 256° long grids. The fourth-order Runge–Kutta method is used for time integrations with a time increment of 1/80 day. We use the analytic form of the forcing originally introduced by Hartmann (1983):

$$\overline{u}_0(\phi) = U \cos\phi \operatorname{sech}\frac{2(\phi - \phi_0)}{B}, \quad (2)$$

where U, B, and ϕ_0 are parameters characterizing the polar night jet—U is a measure of intensity of the jet, B its width, and ϕ_0 its position. It is converted to $\overline{q}_0(\phi)$ in Eq. (1) through the relationship of $\overline{q}_0 = 2\Omega \sin\phi - (a\cos\phi)^{-1} d(\overline{u}_0 \cos\phi)/d\phi$. Three types of solutions, time periodic (steady wave), quasiperiodic (vacillation), and aperiodic (irregular flow) ones, are obtained after long-time integrations in Ishioka and Yoden (1995), depending on these three parameters. Regime diagrams in the three-dimensional parameter space are given in Fig. 1 of Ishioka and Yoden (1995).

The model is integrated from an initial condition of a zonally symmetric state $\overline{u}_0$. Initially a small perturbation is added and the perturbation grows in time if $\overline{u}_0$ is barotropically unstable. After the initial transient period, the flow settles into a state in which the forcing to intensify the unstable jet and the disturbances growing from the instability are balanced. In other words, the time-dependent solution falls into an attractor in phase space—limit cycle for steady wave solution, torus for vacillation, and strange attractor for irregular solution. We investigate the flow after 1000-day integration to avoid the influence of the initial transience. The time given in the figures is reset to zero at day 1000.

Trajectories of many fluid particles are computed simultaneously with the time integration of the flow field. Spectral coefficients of the vorticity field, $q_n^m(t)$ ($0 \le |m| \le n$, $n = 1, 2, \ldots, 85$), and positions of the particles, $\mathbf{x}_i(t)$ ($i = 1, 2, \ldots, I$), are put into the Runge–Kutta routine as one set of variables. The position of

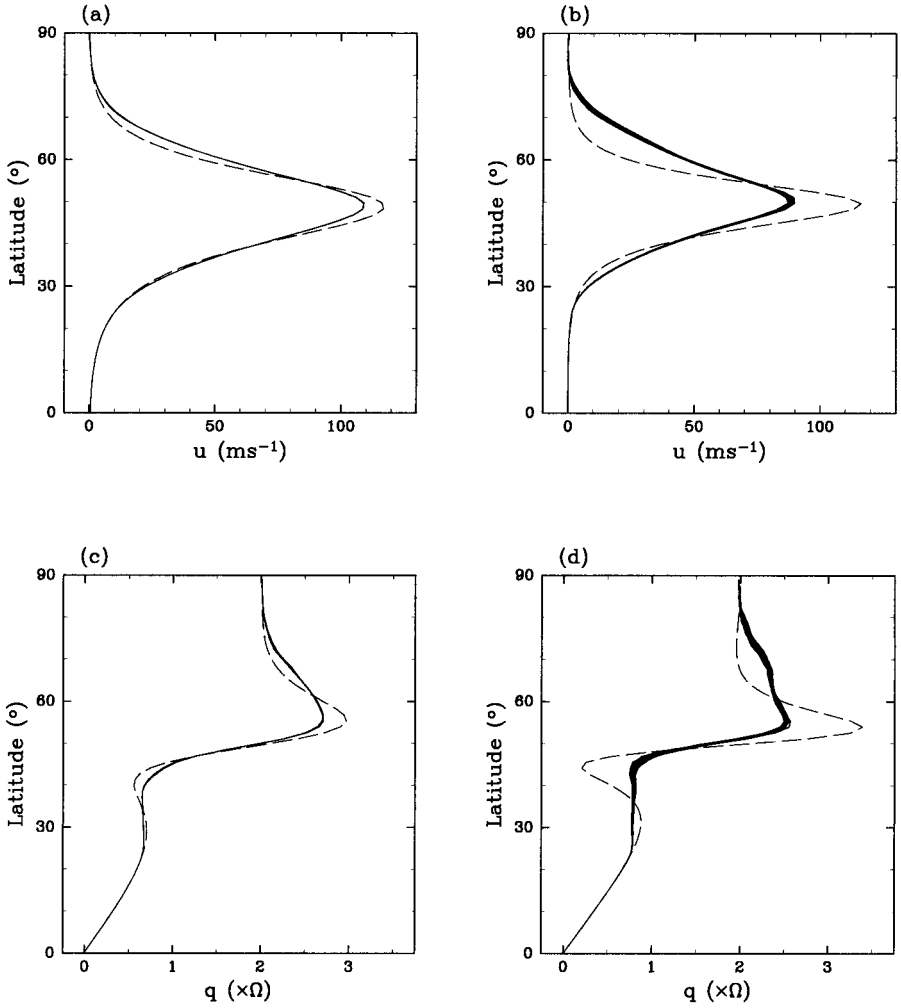

FIG. 1. Zonal mean zonal wind $\overline{u}(\phi)$ and zonal mean PV $\overline{q}(\phi)$ as a function of latitude for (a) and (c) the vacillation and for (b) and (d) the irregular solution. The profiles at every 1/5 vacillation cycle are drawn for the vacillation and at each day of 20 days for the irregular solution. The dashed lines are the prescribed $\overline{u}_0(\phi)$ and $\overline{q}_0(\phi)$.

the ith particle is represented by longitude λ_i and latitude ϕ_i, which are determined by the following equations:

$$\frac{D\lambda_i}{Dt} = \frac{u(\lambda_i, \phi_i, t)}{a\cos\phi_i} = \left[-\frac{1}{a^2\cos\phi}\frac{\partial\psi}{\partial\phi}\right]_{\lambda=\lambda_i,\phi=\phi_i}, \quad (3)$$

$$\frac{D\phi_i}{Dt} = \frac{v(\lambda_i, \phi_i, t)}{a} = \left[\frac{1}{a^2\cos\phi}\frac{\partial\psi}{\partial\lambda}\right]_{\lambda=\lambda_i,\phi=\phi_i}, \quad (4)$$

where ψ can be obtained at anywhere through the inversion of q at each step of the Runge–Kutta scheme.

3. Results

We used two parameter sets, $(U, \phi_0, B) = (180$ m s^{-1}, 50°, 15°) and (180 m s^{-1}, 50°, 10°), in this section. While these parameter sets are close to each other, the solutions are categorized into different regimes: the former parameter set gives a vacillation solution, and the latter gives an irregular one. Some additional results with different parameter sets are also examined in the discussion section.

a. Flow fields

Zonal mean profiles of zonal flow $\overline{u}$ and PV $\overline{q}$ for the vacillation and the irregular solution are shown in Fig. 1. The dashed line represents the prescribed forcing $\overline{u}_0$ and $\overline{q}_0$. These parameter sets produce a narrow jet centered on about $\phi = 50°$ (Figs. 1a,b), where the meridional gradient of $\overline{q}_0$ has its maximum. The gradient of $\overline{q}_0$ is negative around $\phi = 35°$ and 60° (Figs. 1c,d). The prescribed profiles fulfill the necessary condition for barotropic instability on both sides of the jet. The flow after the initial transient period is a nearly balanced state between the forcing and growing disturbances from

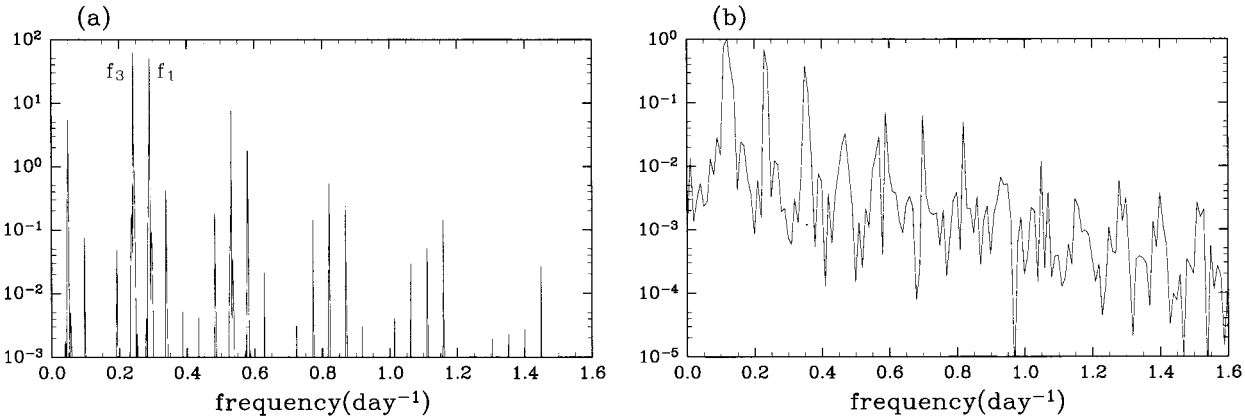

FIG. 2. Power spectrum density of the time series data of PV ($\times\Omega^2$ day) at a point on (λ, ϕ) = (0°, 50°) for (a) the vacillation and (b) the irregular solution.

the instability. The obtained jet is weaker and wider than the prescribed one. The negative gradient of $\overline{q}$ disappears on the equatorial side of the jet, and $\overline{q}$ is nearly constant between $\phi = 25°$ and 40° or 45°. On the other hand, the negative gradient remains on the polar side, although it is weakened.

Figure 2 shows the power spectrum density of the time evolution of PV value at a given position on (λ, ϕ) = (0°, 50°). The time evolution in the vacillation is quasiperiodic, and its spectrum (Fig. 2a) contains only frequencies of $f_1 = 0.290$ day^{-1}, $f_3 = 0.241$ day^{-1} and their linear combinations, $mf_1 \pm nf_3$ (m and n are integers). These frequencies are incommensurable and correspond to the frequency of planetary waves of zonal wavenumber 1 and 3, respectively, as described later. The power spectrum density in the irregular flow is shown in Fig. 2b. It is a continuous one with no specific periodicity. Fluctuation with periods of about 4 and 8 days seems somewhat dominant among the high noise level.

A Hovmöller diagram of $\phi = 50°$ for the vacillation solution is shown in Fig. 3a. Two dominant components are eastward-propagating wavenumbers 1 and 3. Each component is shown in Figs. 3b and 3c. The angular phase speed of wavenumber 1 is $c_1 = 2\pi f_1$, and that of wavenumber 3 is $c_3 = 2\pi f_3/3$. Wavenumbers 1 and 3 are comparable in amplitude and the other components are very small. Amplitudes of these waves are fluctuating with a period of 1.59 day, through the interaction between the waves and the zonal mean zonal flow. Flow field for the vacillation is fundamentally composed of the zonal mean jet and the two planetary waves. Figure 4 is the time evolution of the PV field on the corotating frame with the mean angular speed of wavenumber 1; its rotation period is $1/f_1 = 3.45$ days. Strong horizontal gradient of PV on about $\phi = 50°$ is the edge of the polar vortex, where the jet has its maximum, and PV is roughly constant outside the vortex and close to the zonal mean $\overline{q}$ shown in Fig. 1c. On the corotating frame, wavenumber 3 pattern propagates westward with the mean angular speed of $c_3' = c_3 - c_1$ (e.g., see the innermost contour line with triangular shape). Therefore, the same PV field is repeated at every $2\pi/(3|c_3'|) = 1.59$ days. The quasiperiodicity is regarded as a composition of the vortex rotation with the period of wavenumber 1 (3.45 days) and the periodic variation of its

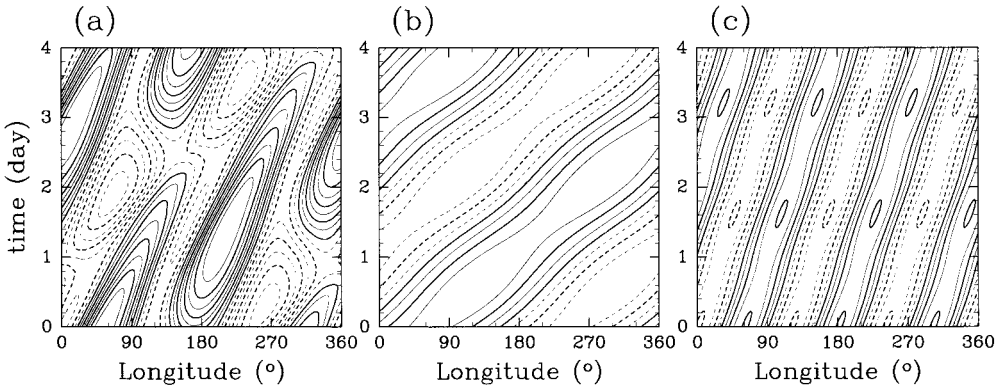

FIG. 3. Hovmöller diagrams of PV on $\phi = 50°$ of (a) all the wave components, (b) wavenumber-1 component, and (c) wavenumber-3 component.

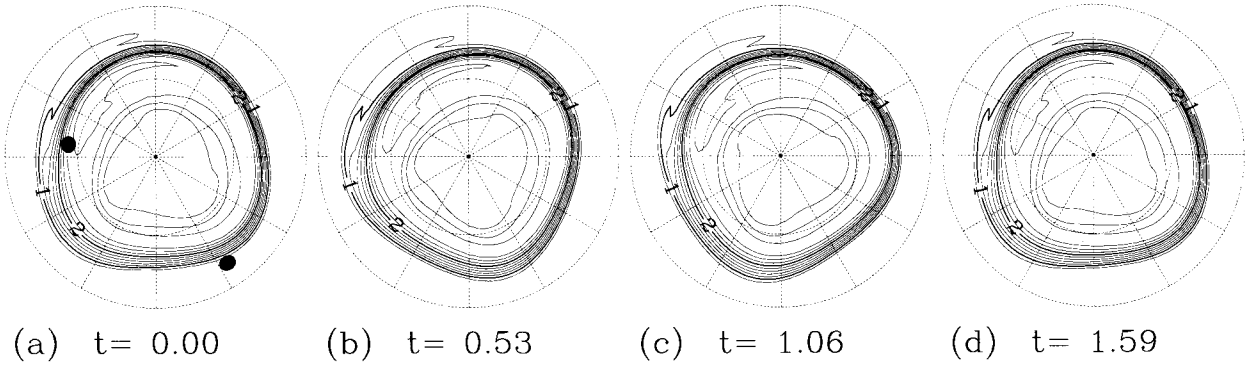

FIG. 4. Time evolution of PV field at every 1/3 vacillation cycle, shown in a corotating frame with the mean angular speed of wavenumber 1 component. Contours are scaled by Ω. The maps are Lambert equal area projections, with the dashed lines of 30° and 60° latitude circles. Small circles in (a) are the initial positions of the particles advected in Fig. 6.

shape with 1.59 days due to the slower phase speed of wavenumber 3. Similar vortex rotation is also seen in the irregular solution (not shown). The rotation period is about 4 days. The PV field shows that planetary waves spontaneously break in the irregular solution but breakings are small enough to keep the vortex shape, while few planetary wave breakings are seen in the vacillation.

b. Finite-time Lyapunov exponents

Finite-time Lyapunov exponent is used as a local and quantitative measure of mixing. The exponent gives the exponential growth rate of the distance between two nearby trajectories. Spatial distributions are examined for some various evaluation times since it depends on initial position and evaluation time. Numerically, the singular vector method (Shimada and Nagashima 1979; Goldhirsch et al. 1987; Geist et al. 1990) is used. Evolution of two orthonormal small perturbations $\delta\mathbf{x}$ from a point $\mathbf{x}$ is calculated for a given evaluation time τ to make a 2×2 matrix $\mathbf{M}$ such that

$$\delta\mathbf{x}(t_0 + \tau) = \mathbf{M}(\mathbf{x}(t_0), \tau)\, \delta\mathbf{x}(t_0). \tag{5}$$

The largest finite-time Lyapunov exponent λ_1 is defined as

$$\lambda_1(\mathbf{x}(t_0), \tau) = \frac{1}{\tau} \log\sigma_1, \tag{6}$$

where σ_1 and σ_2 are the singular values of $\mathbf{M}$ ($\sigma_1 > \sigma_2 > 0$). The pull-back method (Lichtenberg and Lieberman 1992) is used to remove nonlinear effects due to amplification; the perturbations are deflated to 1/10 when one of them grows 10 times larger than the initial amplitude and all deflation factors are multiplied back at the end of the calculation.

Figure 5 shows the spatial distributions of the largest finite-time Lyapunov exponents λ_1 for the vacillation (Figs. 5a,b), and the irregular flow (Figs. 5c,d) for two evaluation times of $\tau = 2$ and 90 days. Calculations are done on every $2° \times 2°$ grid in the latitudes of $\phi \geq 20°$ with two small perturbations of angular length of 10^{-6} rad in longitudinal and latitudinal directions. In the results of $\tau = 2$ days (Figs. 5a and 5c), low value of λ_1 is seen on a ring corresponding to the edge of the polar vortex. Areas of high value are on the both flanks of the ring. The value is higher on the equatorial side than on the polar side. These areas are affected by linear deformation due to horizontal shear. The effect by chaotic behavior of the particles is not clear at this stage because of the short evaluation time. For longer time intervals of $\tau = 90$ days, the ring of low λ_1 at the edge of the polar vortex is less evident in the irregular solution (Fig. 5d), while it is well identified even for $\tau = 90$ days in the vacillation (Fig. 5b). The value inside is lower than outside, which is consistent with previous studies (e.g., Bowman 1993; Bowman and Chen 1994). In the areas of high value, it varies at every grid; since Lagrangian trajectory is sensitive to the initial position, growth of the distance of two trajectories is also sensitive to the initial position. Note also that for both solutions λ_1 is quite low in low latitudes of $\phi \leq 25°$ where PV has positive meridional gradient.

Spatial distributions of λ_1 for the both solutions show large inhomogeneity inside the polar vortex. A large triangular region with round corners in which the value is very low is seen inside the vortex. The region is still discernible in both solutions even $\tau = 90$ days. In addition, a crescent-shaped region with low λ_1 is also seen between the triangular region and the vortex edge identified as large PV gradient, particularly in the vacillation.

Quantitative arguments on the probability distribution functions of the finite-time Lyapunov exponents will be given in the discussion section together with some additional results.

c. Macroscopic dispersion of particles

Two closed circles in Fig. 4a denote the points at which the finite-time Lyapunov exponent for $\tau = 2$ days is highest inside and outside of the vortex, respectively.

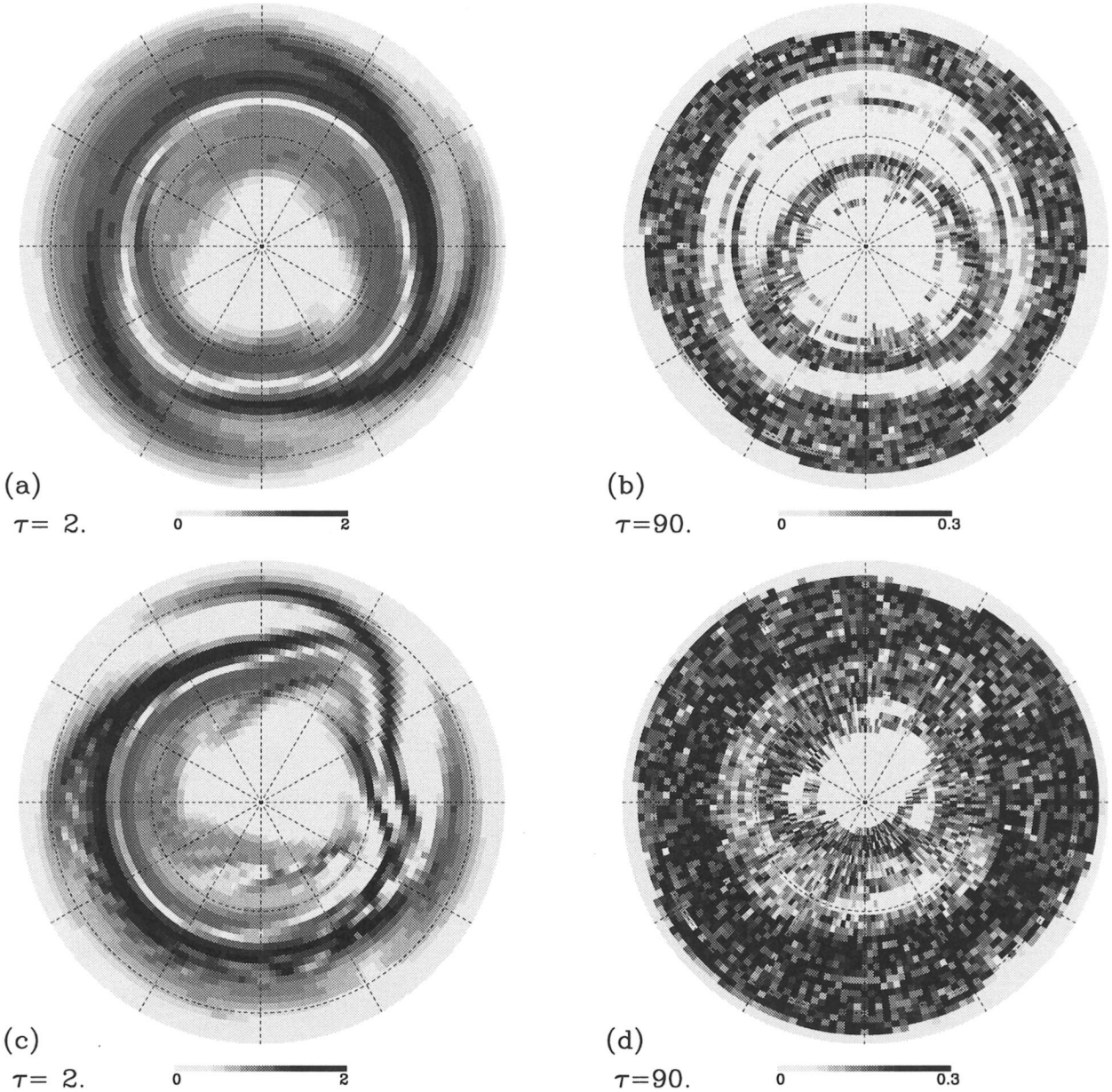

FIG. 5. Distributions of the largest finite-time Lyapunov exponent on a 2° × 2° grid for $\phi \geq 20°$ for (a) and (b) the vacillation and (c) and (d) the irregular solution. Two evaluation times of $\tau = 2$ days and $\tau = 90$ days are used.

Initially we put 10^4 particles randomly in the circle centered on the points with a radius of 0.05 rad, and computed their trajectories for 90 days in order to have fundamental pictures of the mixing process.

Results for the vacillation are shown in Fig. 6. The particles outside the vortex (Figs. 6a–c) are well mixed in 90 days. At first, particles are stretched out to west and east by the meridional shear of the jet. They become distributed on a thin line element surrounding the polar vortex. At the same time, the element is distorted and folded at several places (Fig. 6a). Such stretching and folding processes are repeated and the layered structures of the particles are made (Fig. 6b). They are well mixed within a zone between about $\phi = 25°$ and 45° (Fig. 6c). This is a typical example of chaotic mixing process. The well-mixed zone corresponds to the latitudes with nearly constant PV shown in Fig. 1c. Two transport barriers exist at both boundaries of the chaotic mixing zone. The barrier at the polar-side boundary is on about 45°, not located on the polar vortex edge that is defined as the largest meridional gradient of PV at each longitude. The difference between the barrier and the vortex edge is

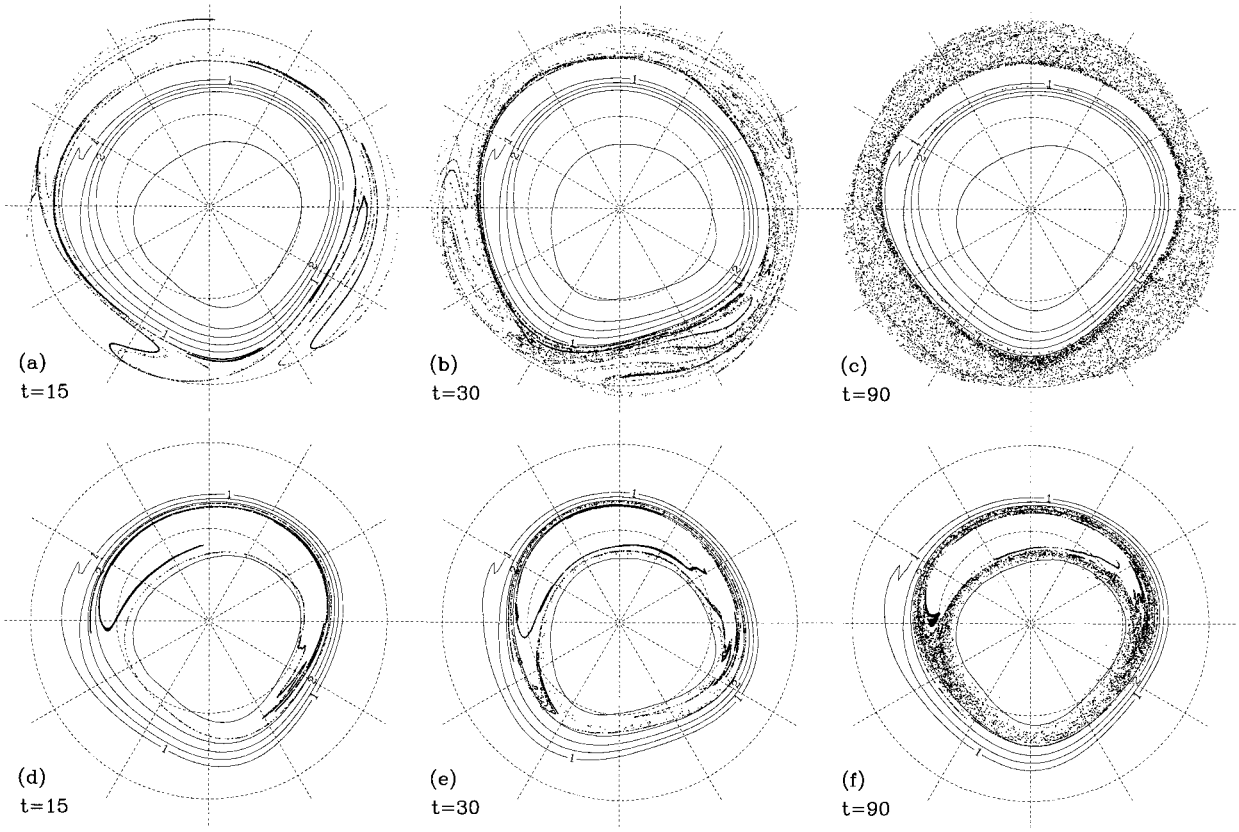

FIG. 6. Advection of 10^4 fluid particles for 90 days in the vacillation from (a)–(c) outside the polar vortex and from (d)–(f) inside, shown in the same corotating frame as for Fig. 4. Initial positions of these particles are shown in Fig. 4a. Contours are the PV field.

about 10° at its maximum. Note that this barrier is not perfect; a small number ($\sim 10^2$) of the particles reach near the vortex edge.

Particles inside the polar vortex are also mixed in a similar way as shown in Figs. 6d–f. But they do not spread all over the vortex inside. Two empty regions exist even at $t = 90$ day (f). The shape of these regions resembles that of low λ_1 shown in Fig. 5b; a triangular region at the core of the vortex and a crescent-shaped region. As described in the previous studies, the edge of the polar vortex behaves as a transport barrier and there is no particle exchange between inside and outside of the vortex in the vacillation.

Figure 7 shows the results for the irregular solution. Stretching and folding processes very similar to those in the vacillation are seen on the both sides of the vortex. Combined with the positive Lyapunov exponents, chaotic mixing dominates the large-scale mixing process. Compared with Fig. 6c, particles outside the vortex (Figs. 7a–c) are mixed in a larger area, and the distribution is more uniform, which is consistent with the results of the finite-time Lyapunov exponents shown in Fig. 5d. The difference between the transport barrier and the vortex edge found in Fig. 6c disappears in the irregular solution; the transport barrier is located just on the vortex edge. Particles inside the vortex (Figs. 7d–f) are mixed more rapidly and more effectively than in the vacillation. However, some empty regions remain even after 90 days, although the areas are much smaller than those in the vacillation. In addition to a triangular region and a crescent-shaped region, three small ''island'' regions surround the triangular region. While planetary wave breaking events make a small amount of the particles go outside of the vortex for 90 days, there are no incoming particles from outside during the period.

d. Correlation dimension

Correlation functions for the particle distributions obtained in section 3c are computed to diagnose the time evolution of the particle dispersion and mixing quantitatively (Pierrehumbert 1991a,b). Two-particle correlation function is computed as the cumulative histogram

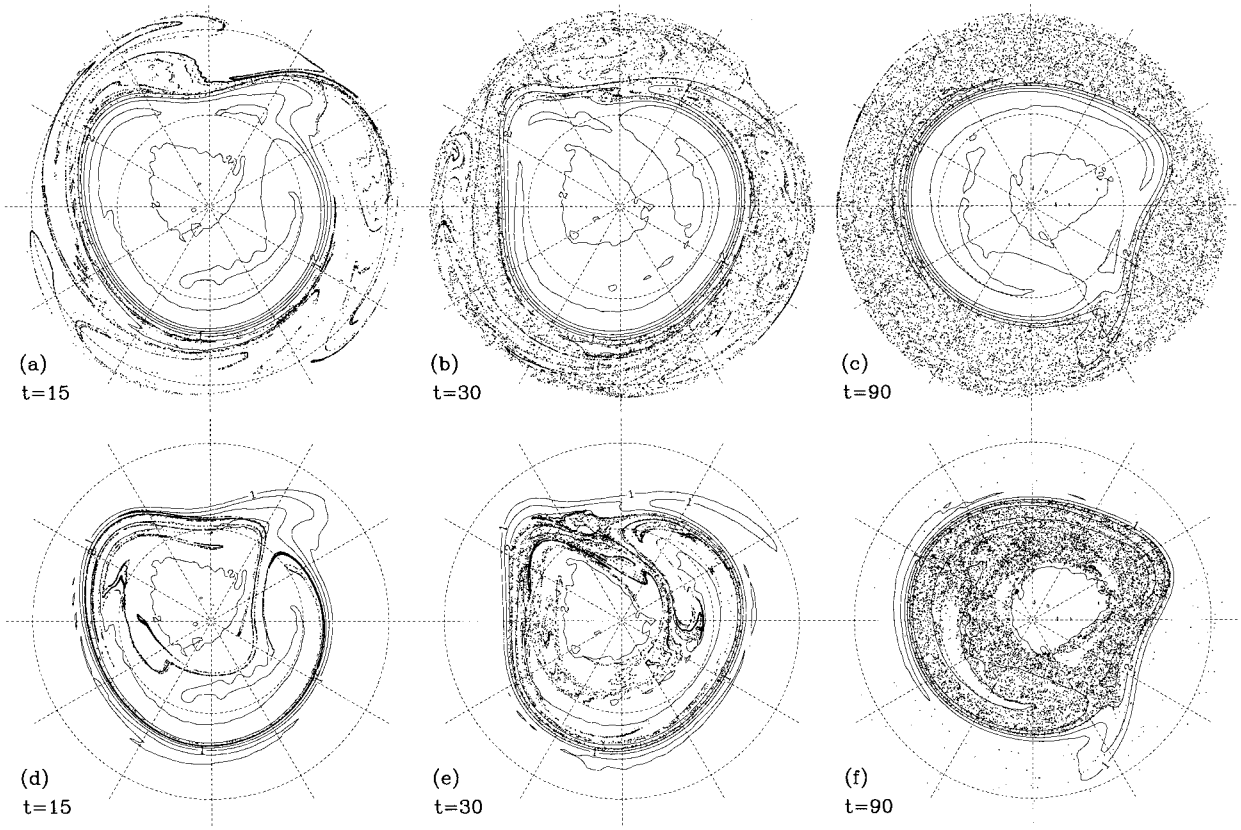

FIG. 7. As in Fig. 6 but for the irregular flow.

$H(r)$ for the distance r between all pairs of the 10^4 particles, and correlation dimension is defined as $d \log H(r)/d \log r$, which gives a fractal dimension of the particle distribution. In two-dimensional flow, well-mixed particles should have a dimension close to 2, while particles aligned on a line have a dimension close to 1. It gives information of the scale on which mixing (or two-dimensionalization of the particle distribution) has occurred. Here we use angular distance φ instead of r on the spherical geometry.

Figures 8a,b show the time evolution of the correlation dimension as a function φ for the particles in the vacillation of Fig. 6. The dimension is 2 at $t = 0$ day for small φ because the initial positions of the particles are random in the small area. Outside the polar vortex in the vacillation (Fig. 8a), the dimension gets closer to 1 within 30 days owing to the initial stretching effect. After that, the dimension increases from 1 to 2, implying that the distribution is approaching two-dimensional. The increase of dimension occurs from larger scales, down to smaller scales; macroscopic mixing precedes microscopic mixing. The dimension estimated at $t = 90$ days is about 1.8 on the scale of $\varphi < 0.2$, which is about the meridional width of the mixing zone. This result is typical of chaotic mixing and has an opposite character from diffusive or turbulent mixing. This is consistent with the kinematical results obtained by Pierrehumbert (1991a,b). On the other hand, such characteristics are not obtained inside the vortex (Fig. 8b). The dimension has little change on the small scale of $\varphi < 10^{-3}$, while that on the larger scale is about 1 for 90 days. It is due to the existence of two large empty regions, which reduce the mixing region.

Time evolutions of the correlation dimension for the irregular flow shown in Figs. 8c,d are not so different between outside and inside. The distributions become close to one-dimensional in 30 days, followed by mixing in the larger scale. The characteristics of chaotic mixing are seen more evidently in this irregular flow than in the vacillation, although the dimension on $\varphi < 10^{-3}$ is 1.5 even after 90 days.

e. Poincaré section

As seen in Fig. 4, the only thing we can see on the corotating frame with wavenumber 1 is the periodic variation of vortex shape with the vacillation period. Poincaré sections are available in this corotating frame. Trajectories of several particles are calculated for a long integration time, and the positions at every one vacillation cycle are all plotted on one figure.

Figure 9 shows the Poincaré sections computed for

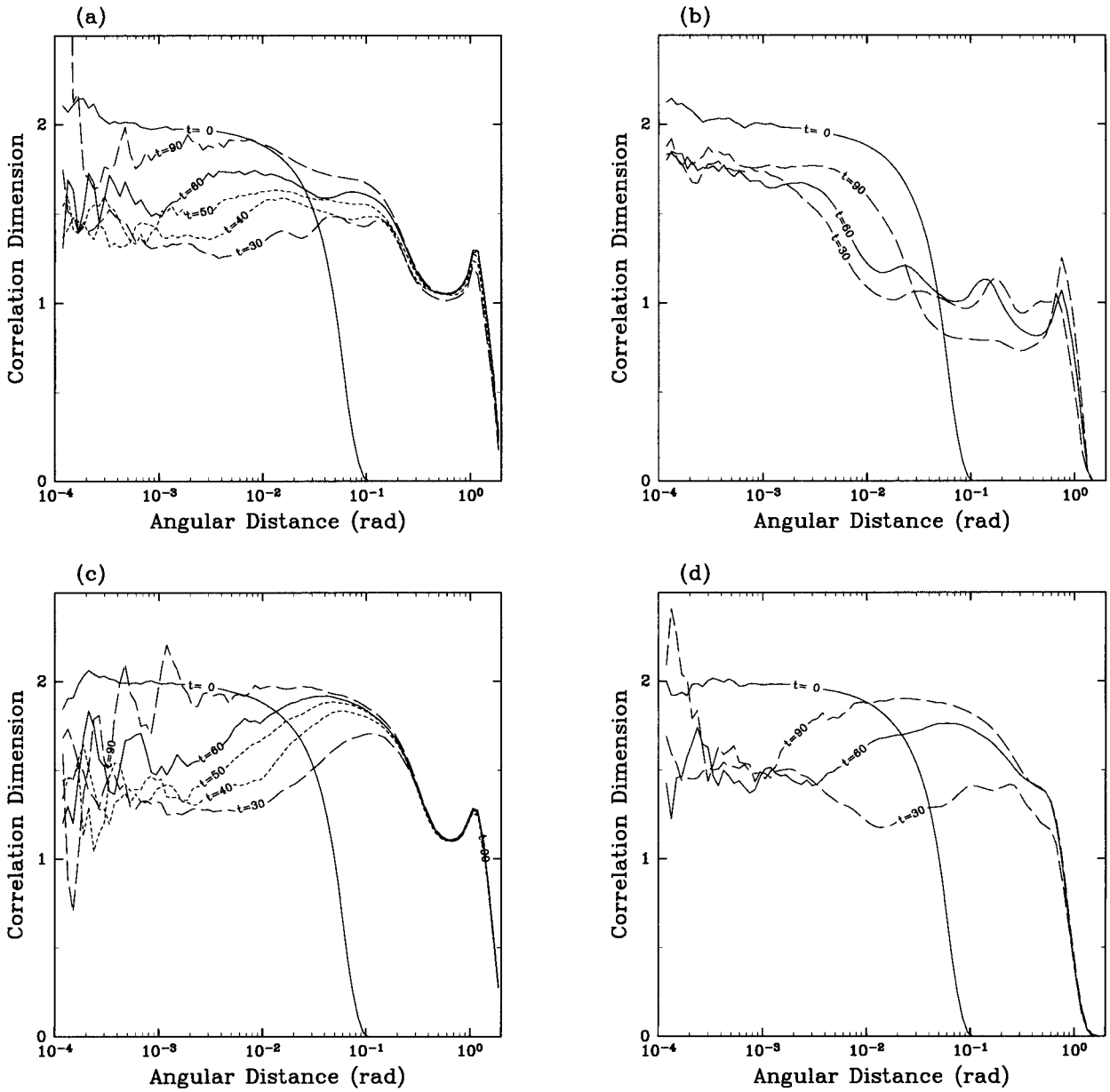

FIG. 8. Correlation dimensions for the particle dispersion shown in Figs. 6 and 7 as a function of the angular distance φ. (a) The vacillation, outside the polar vortex; (b) the vacillation, inside; (c) the irregular flow, outside; and (d) the irregular, inside.

1000 vacillation cycles with 12 particles initially put outside the polar vortex (Fig. 9a), and 19 particles inside the vortex (Fig. 9b). Regions where particles have chaotic, irregular trajectories are the chaotic mixing regions, while regular trajectories are seen in the regions of invariant tori where the fluid is not mixed but only stirred. Outside the polar vortex (Fig. 9a), chaotic mixing region is recognized in midlatitudes. It is wider than the mixing region shown in Fig. 6c because of the longer integration period. Closed dashed lines found at the both sides of the mixing zone are invariant tori. The one inside the mixing zone (blue, dashed line) coincides with steep PV gradient at the polar vortex edge. Another crescent-shaped torus is also found just outside of the edge (red line). Now, the difference between the transport barrier and the vortex edge found in Fig. 6c is explained by the existence of this crescent-shaped torus. Another chaotic mixing region is found inside the polar vortex (Fig. 9b) with more complicated structure of invariant tori. A crescent-shaped torus corresponds to the empty region of similar shape found in Fig. 6f, while the almost empty region of the triangular region in Fig. 6f is filled with chaotic trajectories and three groups of invariant tori: 1) central region of the polar vortex (green, solid loop);

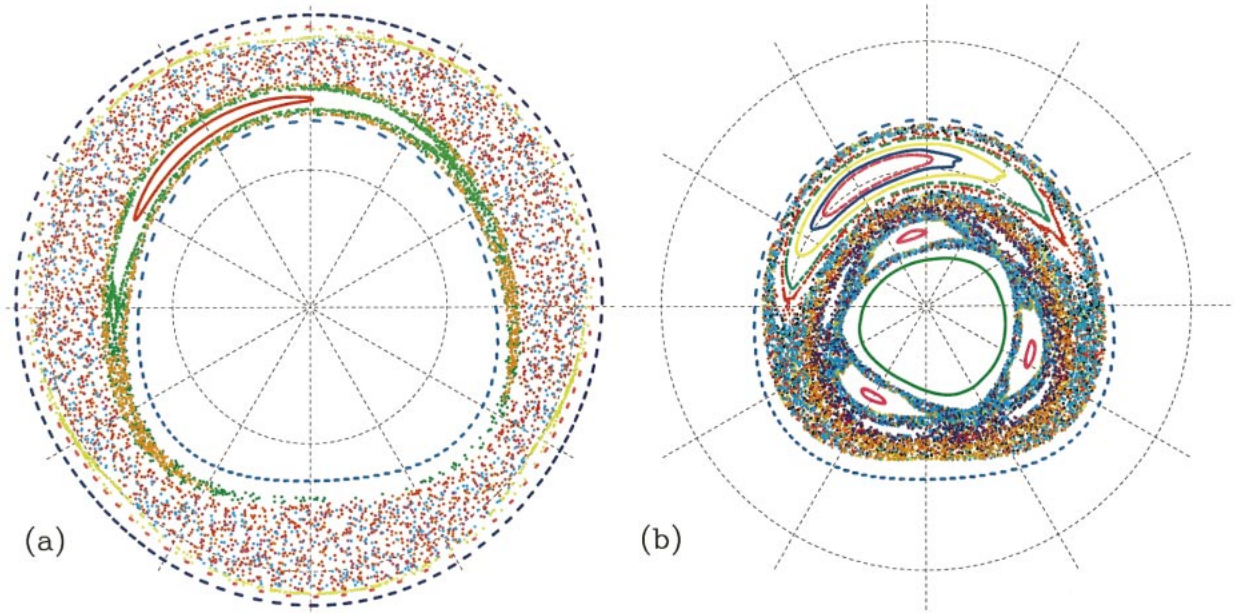

FIG. 9. Poincaré section of the particles for the vacillation with (a) 12 points initially located outside the vortex, and with (b) 19 points located inside.

2) three ''islands'' surrounding the central region, which are identified with three red loops; and 3) four thin islands just outside the three islands. These are transport barriers of different types from the polar vortex edge that are not related to any steep PV gradient.

f. Critical latitudes

Stirring and mixing in a wavy flow field are often explained by the nonlinear behavior of fluid particles in a critical layer. Stagnation points are located on the critical line where the flow speed is identical to the phase speed of a single sinusoidal wave, and trapped regions with closed streamlines connecting the stagnation points are called ''cat's eyes'' (Stewartson 1978; Warn and Warn 1978). Perturbed cat's eyes are the place where stirring and mixing occur. Polvani and Plumb (1992) pointed out that mixing takes place around a stagnation point near the polar vortex. The mixing around the polar vortex is also explained by the existence of critical latitudes of planetary waves in some cases (Bowman 1996).

Although the flow field is more complicated in the present vacillation solution, explanation by stagnation points and cat's eyes on a critical latitude is possible by decomposition into zonal wave components. Figure 10a shows stagnation points and streamlines connecting the points for the zonal mean and wavenumber-1 compo-

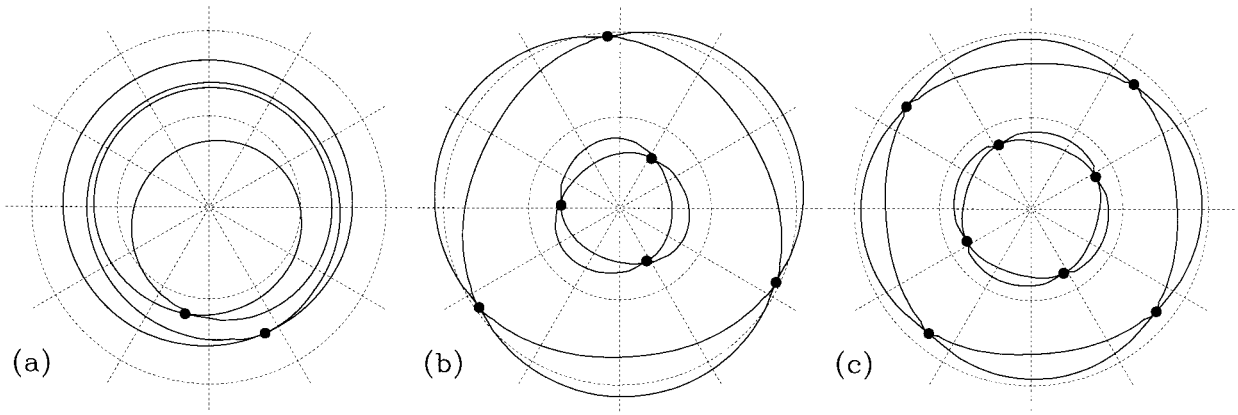

FIG. 10. Stagnation points (bullets) and streamlines connecting the points (thick lines) for the vacillation. These are obtained from the streamfunction field for the zonal mean plus one wave component viewed from an appropriate corotating frame: (a) wavenumber 1 with the frame of angular speed c_1, (b) wavenumber 3 with c_3, and (c) wavenumber 4 with c_4.

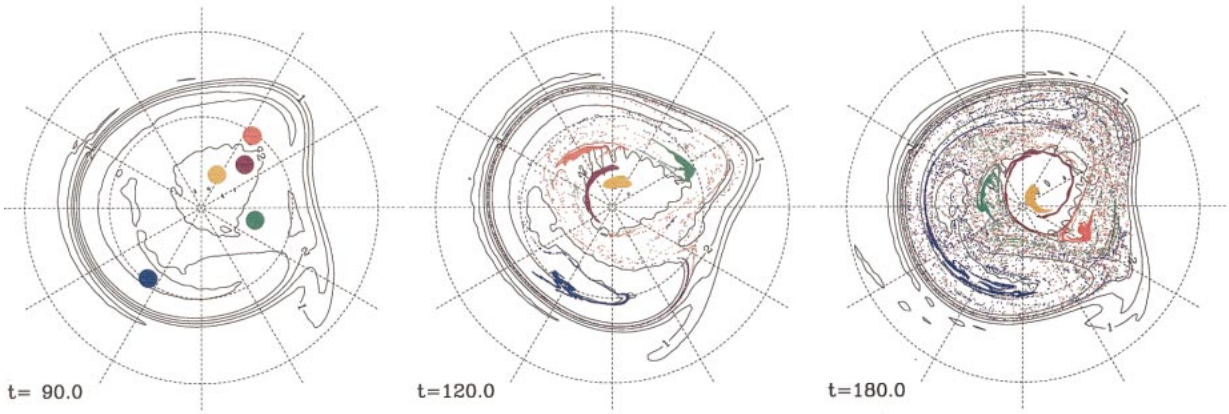

FIG. 11. (a) Advections of fluid particles in the irregular flow initially put at $t = 90$ day. Results at (b) $t = 120$ days and (c) $t = 180$ day are shown.

nents on the comoving frame with c_1, the phase speed of the wavenumber 1 component. Critical latitudes are located on both sides of the jet. Closed streamlines inside the two pairs of homoclinic orbits correspond to two invariant crescent-shaped tori just inside and outside of the vortex edge in Fig. 9. The same plots for wavenumbers 3 and 4 are shown in Figs. 10b,c, respectively. The frequency of the wavenumber 4 is $f_4 = f_1 + f_3 = 0.531\ \text{day}^{-1}$, corresponding to the third highest peak in Fig. 2a. The critical latitude of the wavenumber 3 on the polar side is on about 70°. That of the wavenumber 4, on about 65°, is closer to the jet since $c_3 < c_4 = 2\pi f_4/4$. These two latitudes coincide with the latitudes of three and four islands of invariant tori, respectively, as shown in Fig. 9b. Such island structures corresponding to the cat's eyes on the equatorial side of the jet core are hard to find in the Poincaré section of Fig. 9a.

g. Transport barriers inside the polar vortex

The method of Poincaré section cannot be used for irregular solutions, but some features obtained in the Poincaré section for the vacillation have correspondence with empty regions found in the irregular solution (Fig. 7f); isolation of the central region of the polar vortex, the crescent-shaped region, and the three islands surrounding the central region. The isolation of these regions in the irregular solution is examined by computing dispersion of particles from these regions as shown in Fig. 11. Initial positions of five blobs of 10^4 particles at $t = 90$ day (Fig. 11a) are set in the same manner as in section 3c. The particles put in the very center of the triangular region (orange) do not disperse and stay together in 90 days, and those put in the limb of the triangular region (brown) are elongated to a ring by shear dispersion but are not mixed. Thus, the triangular central region is well isolated from the surroundings inside the polar vortex. When put in the crescent-shaped region (blue), the particles are stretched and a part of them are mixed with the surroundings. However, more than half of them stay in the same region and keep clustered for 90 days. The three small island structures, two of which are marked with red and green particles, are also still discernible after 90 days, although some parts of particles spread out within the polar vortex. The three islands are treated as one torus regime in the Poincaré section, but the fluid particles of the three islands are not mixed up together unless they go out to the mixed region.

4. Discussion

Pierrehumbert (1991a) investigated chaotic mixing in a kinematically determined flow in a channel by computing finite-time Lyapunov exponents and Poincaré sections. The results, Fig. 5 in Pierrehumbert (1991a), show the chaotic mixing regions on both sides of the meandering jet, and several regions of invariant tori are seen in the midst of the chaotic region. It is impossible to find any relationship between these regions and large horizontal gradient in the vorticity field. These invariant tori have correspondence with the central region of the vortex and the crescent-shaped torus inside the polar vortex shown in Fig. 9b. In Pierrehumbert (1991a), these invariant tori are found on both sides of the jet due to the symmetrical channel geometry, while most of them are inside the circumpolar jet in this study due to the spherical geometry.

McIntyre and Palmer (1983) originally used PV maps on an isentropic surface to diagnose large-scale horizontal mixing processes in the winter stratosphere with observational data, and Juckes and McIntyre (1987) did similar diagnosis of planetary wave breaking obtained with one-layer spherical model. When planetary waves break, mixing by two-dimensional turbulent flow takes place outside the polar vortex, which results in homogenization of PV. Meridional gradient of PV becomes large at the boundaries of the mixing zone to sharpen the vortex edge. A transport barrier that obstructs mass exchange between the polar region and the midlatitudes

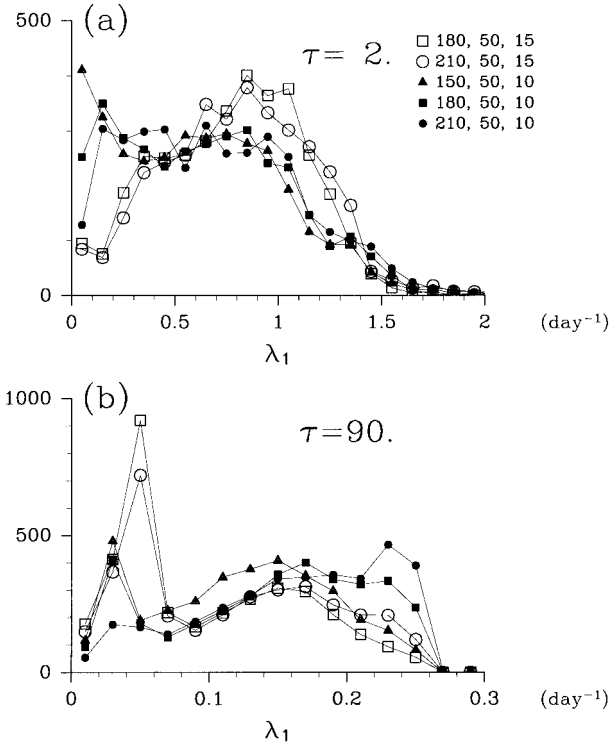

FIG. 12. Histograms of the largest finite-time Lyapunov exponents calculated on $\phi \geq 20°$ for five runs for the parameter sets listed in (a) for U, ϕ_0, and B. The scale of the ordinate is in proportion to the corresponding area since a weight of $\cos\phi$ is multiplied in counting each grid point. Open symbols are for vacillation while closed ones are for irregular solutions.

is produced at the vortex edge with large PV gradient by the planetary wave restoring mechanism. On the other hand, our results provide another situation of producing a transport barrier. Effective mixing occurs in the quasiperiodic vacillation solution without any turbulent, stochastic motion by planetary wave breakings. It should be noted that chaotic mixing in a quasiperiodic solution is possible since PV is not conserved in this forced-dissipative system. Not only a transport barrier corresponding to the large gradient of PV but other isolated regions that are not explained by PV gradient are also found. These kind of transport barriers are located on the boundary between a chaotic mixing region and a regular invariant torus, which was originally found by Pierrehumbert (1991a,b) with a kinematical model. Irregularity of the flow is not the essence of these barriers because they are found in both vacillation and irregular solutions.

In the previous section, various aspects of the mixing process around the polar vortex are compared between the two nearby solutions in the parameter space, that is, the vacillation and the irregular solution. However, time periodicity does not seem to be a unique factor determining the mixing characteristics. For example, the maximum wind speed and meridional shear of the zonal mean jet are rather different between the two solutions as shown in Fig. 1. By three additional runs, we obtained one more vacillation solution for the parameter set of (U, ϕ_0, B) = (210 m s^{-1}, 50°, 15°) and two more irregular one for (150 m s^{-1}, 50°, 10°) and (210 m s^{-1}, 50°, 10°). Histograms of the Lyapunov exponents are made for the distributions shown in Fig. 5 and those for the three additional runs are examined. Note that the histograms are made by multiplying a weight of $\cos\phi$ to the count of grids in order to account for the smaller size of the grid boxes at high latitudes.

Figure 12a shows the histograms for a short evaluation time of $\tau = 2$ days for two vacillation solutions (open marks) and three irregular ones (closed marks). The distribution is different between the two types of solutions; vacillation solutions have a peak near $\lambda_1 = 0.8$, while irregular ones have rather flat distribution for $\lambda_1 < 1.0$. Figures 13a,b shows a high correlation between the mean λ_1 for $\tau = 2$ days and the maximum wind speed, and between the mean λ_1 and the meridional wind shear of the zonal mean jet; the mean Lyapunov

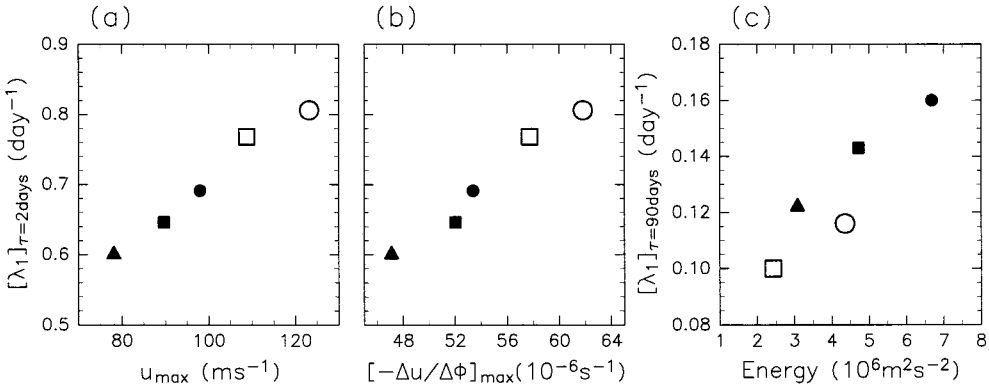

FIG. 13. Relationships (a) between the mean Lyapunov exponents at $\tau = 2$ days and the maximum speed of the zonal mean zonal wind, (b) between the mean Lyapunov exponents at $\tau = 2$ days and maximum horizontal shear inside the vortex, and (c) between the mean Lyapunov exponents at $\tau = 90$ days and total wave energy over the whole region. The symbols are identical to those used in Fig. 12 for the five runs.

exponent is larger as the jet is stronger with larger shear. The correlation becomes low if we take a longer evaluation time. As for such a short time interval, it is plausible to think that the key factor to determine the mixing properties is not the time periodicity but the horizontal shear of the jet.

Some differences are also found between the vacillation and the irregular solutions for a long evaluation time of $\tau = 90$ days as shown in Fig. 12b. Generally there are two peaks near $\lambda_1 = 0.04$ and 0.2. The lower one corresponds to the regular (torus) regions, which shifts to zero as τ increases. On the other hand, cluster of the higher value is associated with the chaotic regions. These distributions are consistent with the results of Pierrehumbert (1991a). The cluster of the higher value is dominant in the irregular solutions. It might be expected that the distribution might be more directly related to the area of chaotic region or amplitude of wave disturbances than the time periodicity. However, Fig. 13c shows that the mean λ_1 for $\tau = 90$ days of the irregular solutions has higher values than those of the vacillation; even when wave energy is the same, mixing in the aperiodic flows is stronger than that in the quasiperiodic flows.

Dynamical systems theory based on Hamiltonian system (Ottino 1989; Wiggins 1992) can be applied to large-scale flow in the stratosphere by idealizing the flow as two-dimensional, quasiperiodic flow. Our results are consistent with the theory that effective, irreversible mixing occurs even when the flow is only vacillating with small amplitude. Poincaré sections determine chaotic mixing regions and invariant tori, which give precise locations of well-mixed regions and transport barriers. Lobe dynamics using stable and unstable manifolds of hyperbolic trajectories around stagnation points is another way of understanding transport and mixing (Malhotra and Wiggins 1998) and it could be applied for the present idealized stratospheric flow.

The atmosphere is influenced by diabatic processes and small-scale three-dimensional turbulence enabling cross-isentropic flow and a departure from the idealized two-dimensional picture studied here. These can change large-scale mixing process quantitatively and qualitatively. Our results will be relevant to the real atmosphere of small departure from the idealized situation such that the variations of planetary waves are nearly periodic and the interactions between the waves do exist but are small. Therefore, the wintertime upper stratosphere in the Southern Hemisphere is an interesting region from the viewpoint we obtained in this study, where the 4-day wave caused by barotropic instability of the polar night jet is dominant and turbulent mixing due to breakings of the planetary waves propagating upward from the troposphere is considerably weak. For applying our results to the real atmosphere, more estimation of the relative importance of the turbulent mixing to the chaotic mixing is required since there are differences in the mixing behavior between the quasiperiodic and aperiodic flows.

5. Conclusions

Chaotic mixing in dynamically consistent flows obtained as numerical solutions of the barotropic vorticity equation was investigated. The barotropic model is a forced-dissipative system that simulates an idealized polar vortex that has similar characteristics to the wintertime upper stratosphere. A quasiperiodic solution and an aperiodic solution were obtained with slightly different parameter values, and the analysis results were compared to examine the usefulness of the concept of chaotic mixing even in more realistic irregular flows.

A typical example of chaotic mixing is obtained for the quasiperiodic flow. Effective, irreversible mixing occurs through stretching and folding process outside of the polar vortex, and inside as well (Fig. 6). As described in the previous studies of the polar vortex (e.g., Bowman and Chen 1994), the mixing process is characterized quantitatively by positive values of Lyapunov exponents (Figs. 5 and 12), and one transport barrier coincides with the edge of the polar vortex where the PV gradient is large. However, transport barriers that are not related to the steep PV gradient are found inside the polar vortex. These are identified more precisely with the isolated island structures (invariant tori) in the Poincaré sections (Fig. 9). They are situated around the critical latitudes for the dominant planetary wave components of the vacillation. These planetary waves are excited by forcing toward a barotropically unstable state. Fluid is isolated within the cat's eye structures along each critical line, but particles around the islands, in the chaotic zones, are mixed by fluctuations of the cats' eyes.

Our results are obtained in a dynamical simulation of the polar vortex, while a similar isolated pattern is also seen in the kinematical study of Pierrehumbert (1991a). Such a finescale structure is only inside the polar vortex, because of the asymmetry due to our spherical geometry. Furthermore, it is revealed that the structure obtained in the quasiperiodic flow is relevant to flows that are weakly aperiodic (Fig. 7). Isolation of several regions inside of the polar vortex is confirmed by the additional experiment of particle dispersion (Fig. 11). Correlation dimension in the irregular solution shows more typical evolution of the chaotic mixing (Fig. 8). And even when wave energy is the same, finite-time Lyapunov exponents become higher in the irregular solution than in the vacillation (Figs. 12, and 13).

Acknowledgments. We thank Dr. K. Ishioka for his efficient library package of the barotropic model with the spectral transform method in the spherical domain (Ishioka 1999). We also thank three anonymous reviewers for their comments and suggestions, which have greatly improved the original manuscript. GFD-DENNOU Library was used for drawing the figures (SGKS

Group 2000). Computations were done at the Data Processing Center, Kyoto University. This work was supported in part by the Grant-in-Aid for Scientific Research of the Ministry of Education, Science, Sports and Culture of Japan, and by the Grant-in-Aid for the Research for the Future Program ''Computational Science and Engineering'' of the Japan Society for the Promotion of Science.

REFERENCES

Allen, D. R., J. L. Stanford, L. S. Elson, E. F. Fishbein, L. Froidevaux, and J. W. Waters, 1997: The 4-day wave as observed from the *Upper Atmosphere Research Satellite* Microwave Limb Sounder. *J. Atmos. Sci.,* **54,** 420–434.

Aref, H., 1984: Stirring by chaotic advection. *J. Fluid Mech.,* **143,** 1–21.

Bowman, K. P., 1993: Large-scale isentropic mixing properties of the Antarctic polar vortex from analyzed winds. *J. Geophys. Res.,* **98,** 23 013–23 027.

——, 1996: Rossby wave phase speeds and mixing barriers in the stratosphere. Part I: Observations. *J. Atmos. Sci.,* **53,** 905–916.

——, and P. Chen, 1994: Mixing by barotropic instability in a nonlinear model. *J. Atmos. Sci.,* **51,** 3692–3705.

del-Castillo-Negrete, D., and P. J. Morrison, 1993: Chaotic transport by Rossby waves in shear flow. *Phys. Fluids,* **A5,** 948–965.

Duan, J., and S. Wiggins, 1996: Fluid exchange across a meandering jet with quasiperiodic variability. *J. Phys. Oceanogr.,* **26,** 1176–1188.

Geist, K., U. Parlitz, and W. Lauterborn, 1990: Comparison of different methods for computing Lyapunov exponents. *Prog. Theor. Phys.,* **83,** 875–893.

Goldhirsch, L., P.-L. Sulem, and S. A. Orszag, 1987: Stability and Lyapunov stability of dynamical systems: A differential approach and a numerical method. *Physica,* **27D,** 311–337.

Hartmann, D. L., 1983: Barotropic instability of the polar night jet stream. *J. Atmos. Sci.,* **40,** 817–835.

Ishioka, K., cited 1999: Ispack-0.3 (in Japanese). [Available online at http://www.gfd-dennou.org/arch/ispack/.]

——, and S. Yoden, 1995: Non-linear aspects of a barotropically unstable polar vortex in a forced-dissipative system: Flow regimes and tracer transport. *J. Meteor. Soc. Japan,* **73,** 201–212.

Juckes, M. N., and M. E. McIntyre, 1987: A high-resolution one-layer model of breaking planetary waves in the stratosphere. *Nature,* **328,** 590–596.

Lichtenberg, A. J., and M. A. Lieberman, 1992: *Regular and Chaotic Dynamics.* 2d ed. Springer Verlag, 692 pp.

Malhotra, N., and S. Wiggins, 1998: Geometric structures, lobe dynamics, and Lagrangian transport in flows with aperiodic time-dependence, with applications to Rossby wave flow. *J. Nonlinear Sci.,* **8,** 401–456.

Manney, G. L., T. R. Nathan, and J. L. Stanford, 1988: Barotropic stability of realistic stratospheric jets. *J. Atmos. Sci.,* **45,** 2545–2555.

——, Y. J. Orsolini, H. C. Pumphrey, and A. E. Roche, 1998: The 4-day wave and transport of *UARS* tracers in the austral polar vortex. *J. Atmos. Sci.,* **55,** 3456–3470.

McIntyre, M. E., 1989: On the Antarctic ozone hole. *J. Atmos. Terr. Phys.,* **51,** 29–43.

——, and T. N. Palmer, 1983: Breaking planetary waves in the stratosphere. *Nature,* **305,** 593–600.

Ngan, K., and T. G. Shepherd, 1997: Chaotic mixing and transport in Rossby-wave critical layers. *J. Fluid Mech.,* **334,** 315–351.

Orsolini, Y., and P. Simon, 1995: Idealized life cycles of planetary-scale barotropic waves in the middle atmosphere. *J. Atmos. Sci.,* **52,** 3817–3835.

Ottino, J. M., 1989: *The Kinematics of Mixing: Stretching, Chaos, and Transport.* Cambridge University Press, 364 pp.

Pierce, R. B., and T. D. Fairlie, 1993: Chaotic advection in the stratosphere: Implications for the dispersal of chemically perturbed air from the polar vortex. *J. Geophys. Res.,* **98,** 18 589–18 595.

——, ——, W. L. Grose, R. Swinbank, and A. O'Neill, 1994: Mixing processes within the polar night jet. *J. Atmos. Sci.,* **51,** 2957–2972.

Pierrehumbert, R. T., 1991a: Large-scale horizontal mixing in planetary atmospheres. *Phys. Fluids,* **A3,** 1250–1260.

——, 1991b: Chaotic mixing of tracer and vorticity by modulated travelling Rossby waves. *Geophys. Astrophys. Fluid Dyn.,* **58,** 285–319.

Polvani, L. M., and R. A. Plumb, 1992: Rossby wave breaking, microbreaking, filamentation, and secondary vortex formation: The dynamics of a perturbed vortex. *J. Atmos. Sci.,* **49,** 462–476.

Samelson, R. M., 1992: Fluid exchange across a meandering jet. *J. Phys. Oceanogr.,* **22,** 431–440.

Schoeberl, M. R., and D. L. Hartmann, 1991: The dynamics of the stratospheric polar vortex and its relation to springtime ozone depletions. *Science,* **251,** 46–52.

——, L. R. Lait, P. A. Newman, and J. E. Rosenfield, 1992: The structure of the polar vortex. *J. Geophys. Res.,* **97,** 7859–7882.

SGKS Group, cited 2000: DCL-5.1. (in Japanese). [Available online at http://www.gfd-dennou.org/library/dcl/.]

Shimada, I., and T. Nagashima, 1979: A numerical approach to ergodic problem of dissipative dynamical systems. *Prog. Theor. Phys.,* **61,** 1605–1616.

Stewartson, K., 1978: The evolution of the critical layer of a Rossby wave. *Geophys. Astrophys. Fluid Dyn.,* **9,** 185–200.

Venne, D. E., and J. L. Stanford, 1979: Observation of a 4-day temperature wave in the polar winter stratosphere. *J. Atmos. Sci.,* **36,** 2016–2019.

Warn, T., and H. Warn, 1978: The evolution of a nonlinear critical level. *Stud. Appl. Math.,* **59,** 37–71.

Waugh, D. W., and Coauthors, 1994: Transport out of the lower stratospheric Arctic vortex by Rossby wave breaking. *J. Geophys. Res.,* **99,** 1071–1088.

Wiggins, S., 1992: *Chaotic Transport in Dynamical Systems.* Springer Verlag, 301 pp.